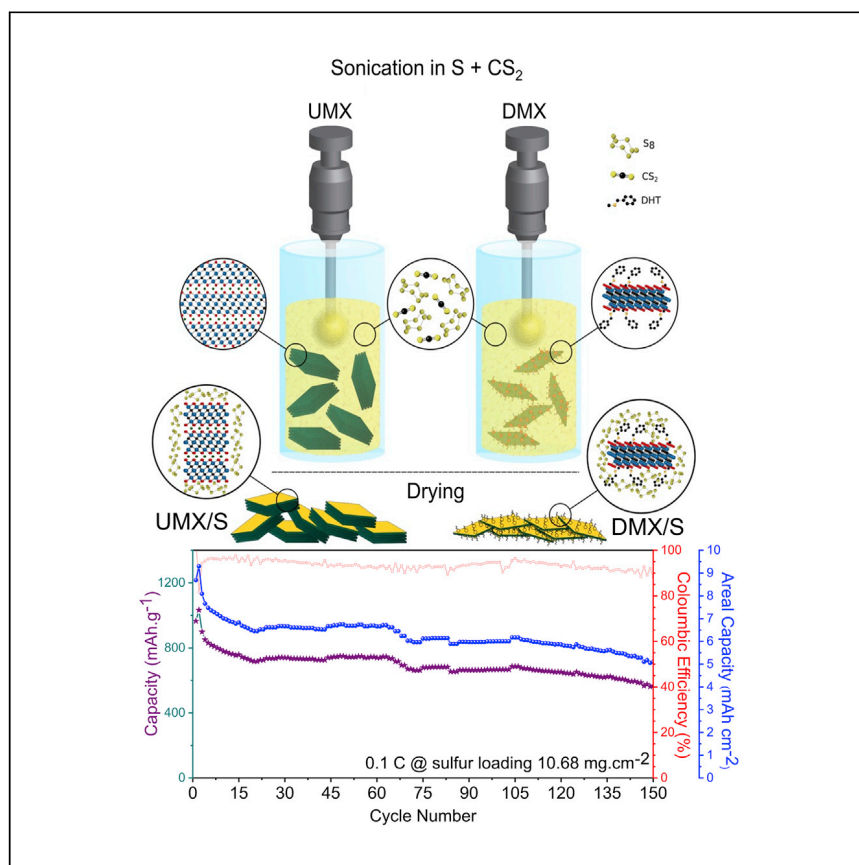


Article

Tuning functional two-dimensional MXene nanosheets to enable efficient sulfur utilization in lithium-sulfur batteries



Rechargeable lithium-sulfur (Li-S) batteries have the potential to replace lithium-ion batteries because of their higher specific energy. Pai et al. report a surface functionalization strategy to enable maximum sheet-surface area use of 2D-MXenes in Li-S batteries, which enables high sulfur loading, capacity retention, and long cycle life.

Rahul Pai, Varun Natu, Maxim Sokol, Michael Carey, Michel W. Barsoum, Vibha Kalra

barsoumw@drexel.edu (M.W.B.)
vk99@drexel.edu (V.K.)

Highlights

DHT functionalized hydrophobic MXenes (DMX) form a stable colloidal solution in CS₂

Atomically thin, metallically conductive DMX improves sulfur utilization in composites

DMX/S cathode delivers good cycling stability at a high sulfur loading of 10.7 mg·cm⁻²

Emphasis on cathode development, pouch-cell performance, and nature of the interactions

Pai et al., Cell Reports Physical Science 2, 100480

July 21, 2021 © 2021 The Authors.

<https://doi.org/10.1016/j.xcrp.2021.100480>



Article

Tuning functional two-dimensional MXene nanosheets to enable efficient sulfur utilization in lithium-sulfur batteries

Rahul Pai,^{1,4} Varun Natu,^{2,4} Maxim Sokol,³ Michael Carey,² Michel W. Barsoum,^{2,*} and Vibha Kalra^{1,5,*}

SUMMARY

Practicality of lithium-sulfur batteries is severely hindered by the notorious polysulfide-shuttle phenomenon, leading to rapid capacity fade. This issue is aggravated with increase in sulfur loading, causing low-coulombic efficiency and cycle life. Herein, we present a facile strategy to combine hydrophobic sulfur and hydrophilic, conductive $\text{Ti}_3\text{C}_2\text{T}_z$ -MXene via one-step surface functionalization using di(hydrogenated tallow)benzylmethyl ammonium chloride (DHT). The latter renders the $\text{Ti}_3\text{C}_2\text{T}_z$ surface hydrophobic, making it readily dispersible in sulfur dissolved in a carbon disulfide (CS_2) solvent. By evaporating the solvent, we conformally coat the DHT- $\text{Ti}_3\text{C}_2\text{T}_z$ (DMX) with sulfur. The developed composite, with higher available active area, enables effective trapping of lithium polysulfides (LiPs) on the electroactive sites within the cathode, leading to improvement in electrochemical performance at higher sulfur loadings. The DMX/S cathodes function with high sulfur loading of $\sim 10.7 \text{ mg} \cdot \text{cm}^{-2}$ and deliver a stable areal capacity of $\sim 7 \text{ mAh} \cdot \text{cm}^{-2}$ for 150 cycles. Moreover, a DMX/S cathode in a pouch-cell configuration retains $\sim 770 \text{ mAh} \cdot \text{g}^{-1}$ after ~ 200 cycles at 0.2C (85.5% retention). *Ex situ* studies elucidate the nature of the LiPs-MXene interaction and the effect of surface functionalization towards improved performance.

INTRODUCTION

The ever-increasing demand and reliability of portable electronic devices and electric vehicles require advanced rechargeable batteries that are cheap, lightweight, and durable.¹ Among several possible options, the lithium-sulfur (Li-S) battery is a promising candidate to satisfy the aforementioned requirements and has the potential to replace the traditional lithium-ion batteries.^{2,3} Elemental S is earth abundant, environmentally benign, low cost, and possesses a high theoretical capacity of $1,675 \text{ mAh} \cdot \text{g}^{-1}$.^{4,5} However, the practicality has been largely hindered because of the shuttle effect, which leads to rapid capacity loss and low coulombic efficiency (CE).⁵ During the charge-discharge cycles, solid S converts to solid Li_2S and vice versa via the formation of soluble lithium polysulfides (LiPs), reaction intermediates.⁶ These LiPs dissolve in the electrolyte shuttle back and forth between the sulfur cathode and lithium anode, leading to a loss of active material, which, in turn, reduces capacity.^{7,8} Furthermore, the dissolution results in the chemical reduction of LiPs on the surface of Li, forming a layer of insulating Li_2S , leading to polarization, and hampering the accessibility of Li^+ ions.⁸ Efforts in the past have focused on mitigating the shuttle effect via the development of high surface area carbonaceous materials to physically contain the LiPs in the cathode hosts.^{9–12} However, the long-term

¹Department of Chemical and Biological Engineering, Drexel University, Philadelphia, PA 19104, USA

²Department of Materials Science and Engineering, Drexel University, Philadelphia, PA 19104, USA

³Department of Materials Science and Engineering, Tel Aviv University, Ramat Aviv 6997801, Israel

⁴These authors contributed equally

⁵Lead contact

*Correspondence: barsoumw@drexel.edu (M.W.B.), vk99@drexel.edu (V.K.)

<https://doi.org/10.1016/j.xcrp.2021.100480>



cycling of such cells remains a prominent issue because of the poor interfacial contact of the polar LiPs with the weakly polar carbon surfaces.¹³

Recently, cathode hosts with strong physical and chemical interactions toward LiPs have shown improvement in capacity retention by suppressing the shuttle phenomenon. Polar metal oxides, such as TiO₂, V₂O₅, Fe₂O₃, Al₂O₃, and SiO₂ show this behavior because their surface oxygen binds LiPs by polar-polar interaction (S₂^{x-}-O-metal).^{13,14} However, the inherent semi-conductive or insulating nature of these host materials impedes electron transport and overall use of the sulfur during the redox process reducing the deliverable capacity. On the other hand, it was reported that non-stoichiometric metal oxides, sulfides, and metal-organic frameworks (MOFs) have the highest affinity toward LiPs because of the Lewis-acid-base bonding (binding energy >3.5 eV).¹⁵ The metallic centers of the non-stoichiometric metal oxides/sulfides have free d-orbitals, which can form a co-ordinate bond with a weakly basic S_x²⁻ anion.¹⁶ In addition, the improved conductivity from metal-metal bonding in non-stoichiometric metal oxides helps provide better electron transport.^{17,18,19} In addition, host conductivity can further boost the conversion of the redox reaction on the surface, mitigating the shuttle effect and improving cycle life.^{20,21}

MXenes are a new class of two-dimensional (2D) carbides and/or nitrides discovered in 2011 by Naguib et al.²² These 2D materials are so called because they are derived by selectively etching A (group 13 or 14 elements) from the parent MAX phase in aqueous acid and organic solvents.²³⁻²⁵ MXenes have a general formula M_{n+1}X_nT_z, where M stands for an early transition metal, X stands for C or N, and T_z stands for chemical terminations, such as -O, -OH, and -F surface groups that replace the Al atoms upon etching.²⁶ Ti₃C₂T_z MXene, obtained by etching Ti₃AlC₂, has shown unique properties, such as high metallic conductivity (>5,000 S·cm⁻¹), and it is environmentally friendly.^{27,28} Furthermore, the developed MXene can be tuned with various surface functional groups, as required for its applications, adding to its versatility.^{29,30}

This unique surface environment with tunable functional groups renders MXene surfaces sensitive to LiPs.^{31,32} Liang et al.³³ have shown that the LiPs bind to MXene host surfaces via a Lewis-acid-base interaction. In addition, the terminal groups form a thiosulfate/polythionate complex, providing better entrapment of LiPs and enabling improved electrochemical performance.³⁴ Incorporating MXenes as a host material has been shown to significantly enhance the charge storage capacity in Li-S batteries. For example, Liang et al.³³ demonstrated the use of MXene/S composite with a high initial capacity of ~1,200 mAh·g⁻¹ at ~1.5 mg·cm⁻² S loading.³⁴ In addition, Bao et al.³⁵ showed that Ti₃C₂T_x/S delivered a capacity of ~1,000 mAh·g⁻¹ with a 1.5 mg·cm⁻² S loading. However, this performance dropped to ~400 mAh·g⁻¹ within 200 cycles. This low capacity was attributed to a lack of porosity because of an intrinsic sheet-like morphology.

To increase capacity retention over cycling, Bao et al.³⁵ used a facile strategy to develop crumpled nitrogen-doped MXenes to improve the porosity of the MXene sheets, enabling a capacity of 900 mAh·g⁻¹ at 0.2C for 200 cycles. Similarly, Song et al.³⁶ developed porous MXene-rGO aerogels, facilitating better ion-transport channels with efficient LiP adsorption, resulting in a cycling stability of 500 cycles, with a deliverable capacity of 600 mAh·g⁻¹.^{36,37} Interestingly, employing MXene sheets alone yields a low electrochemical performance with the S loadings of ~1 mg.^{35,37,38} The better electrochemical performance was observed with the

crumpling of MXene nanosheets, composite aerogel, and a nanodot formation. Such architecture resulted in better ionic transport and a greater accessible surface area. However, the performance was impeded with improvements in sulfur loading. For example, Song et al.³⁶ developed rGO·MXene aerogel composites, delivering cycling stability for 500 cycles at low S loadings and 30 cycles with $\sim 6 \text{ mg}\cdot\text{cm}^{-2}$ S loading. Similarly, Xiao et al.³⁹ developed MXene nanodots, which demonstrated cycling stability of 400 cycles at low loadings. Increasing the loading to $9.2 \text{ mg}\cdot\text{cm}^{-2}$ resulted in stability for only 100 cycles. This reduction in capacity retention can be attributed to lower exposure of active surface terminations and underuse of the conductive MXene sheet surface itself. In addition, the development of such morphology/surface architecture is a multi-step process involving time-consuming high-temperature and pressure treatments.

During the fabrication of S electrodes, a common strategy employed is slurry mixing.^{35,38,39} However, because the MXene surfaces are hydrophilic ($-\text{O}/-\text{OH}$ terminations) and S is hydrophobic, the former tends to re-stack without S depositing on their surfaces. As a result, the overall usable area is reduced, rendering most of the MXene surface area and functional groups redundant for S binding and re-deposition. In addition, most of the interlayer surface is not used during the charge-discharge step. Instead, only the exterior surface of multi-layered MXenes contributes toward LiPs binding, thereby reducing the deliverable capacity and continued shutting in subsequent cycles. Furthermore, most of the previous work employed a heat-melt diffusion strategy at $\sim 150^\circ\text{C}$ – 160°C , usually for 12 h on temperature-sensitive, oxidation-prone MXene surfaces.^{35,38} Therefore, the ideal host-structure model of the MXene-S host cathodes should involve the dispersion of single-layered MXene nanosheets in an S-saturated environment. This architecture can provide efficient diffusion of S within the sheets without temperature treatment, improving the effective use of the surface groups to bind the LiPs in the final cathode.

Herein, we put forward a rational design strategy for employing MXenes as host materials in Li-S batteries. The MXene nanosheets are first surface engineered, allowing them to be dispersed in non-polar solvents, using an inexpensive and industrially relevant di(hydrogenated tallow)benzyl methyl ammonium chloride (DHT) surfactant molecule. These DHT-treated MXene nanosheets, henceforth referred to as DMX, are, in turn, easily dispersed into single to few-layer MXenes in carbon disulfide (CS_2), forming a stable colloidal suspension. The purpose of this work is to demonstrate a simple, single-step strategy for efficient use of the MXene sheet surface, enabling greater S use with improved binding ability, boosting cycling performance. Therefore, the developed DMX cathode delivers a high initial capacity of $1,220 \text{ mAh}\cdot\text{g}^{-1}$ at 0.1C. At a higher rate of 0.5C, these cathodes stabilize at $880 \text{ mAh}\cdot\text{g}^{-1}$ after the first five cycles; 85% of which is still retained after 500 cycles. In addition, to demonstrate practical value, we are developing cathodes with high sulfur loading of $\sim 10.7 \text{ mg}\cdot\text{cm}^{-2}$, which exhibit an initial capacity of $\sim 1,000 \text{ mAh}\cdot\text{g}^{-1}$ and a stable areal capacity of $\sim 7 \text{ mAh}\cdot\text{cm}^{-2}$ for 150 cycles at 0.1C. For comparison, the highest areal capacity exhibited by state-of-the-art Li-ion battery devices is less than $4 \text{ mAh}\cdot\text{cm}^{-2}$. Furthermore, at a high current rate of 1C, the cathode delivers an initial capacity of $\sim 720 \text{ mAh}\cdot\text{g}^{-1}$ and retains around 80% of its capacity after 500 cycles. The improved interfacial contact between DMX and sulfur results in increased utilization, thereby demonstrating stable electrochemical performance for 300 cycles at 83.33 wt% loading. We also demonstrate pouch-cell-level performance with 60 mg of sulfur loading, delivering an initial stable capacity of $900 \text{ mAh}\cdot\text{g}^{-1}$ after five cycles and $770 \text{ mAh}\cdot\text{g}^{-1}$ after ~ 200 cycles, retaining 85.5% capacity. Postmortem analysis of the cycled cathodes further shows the nature of interactions exhibited between

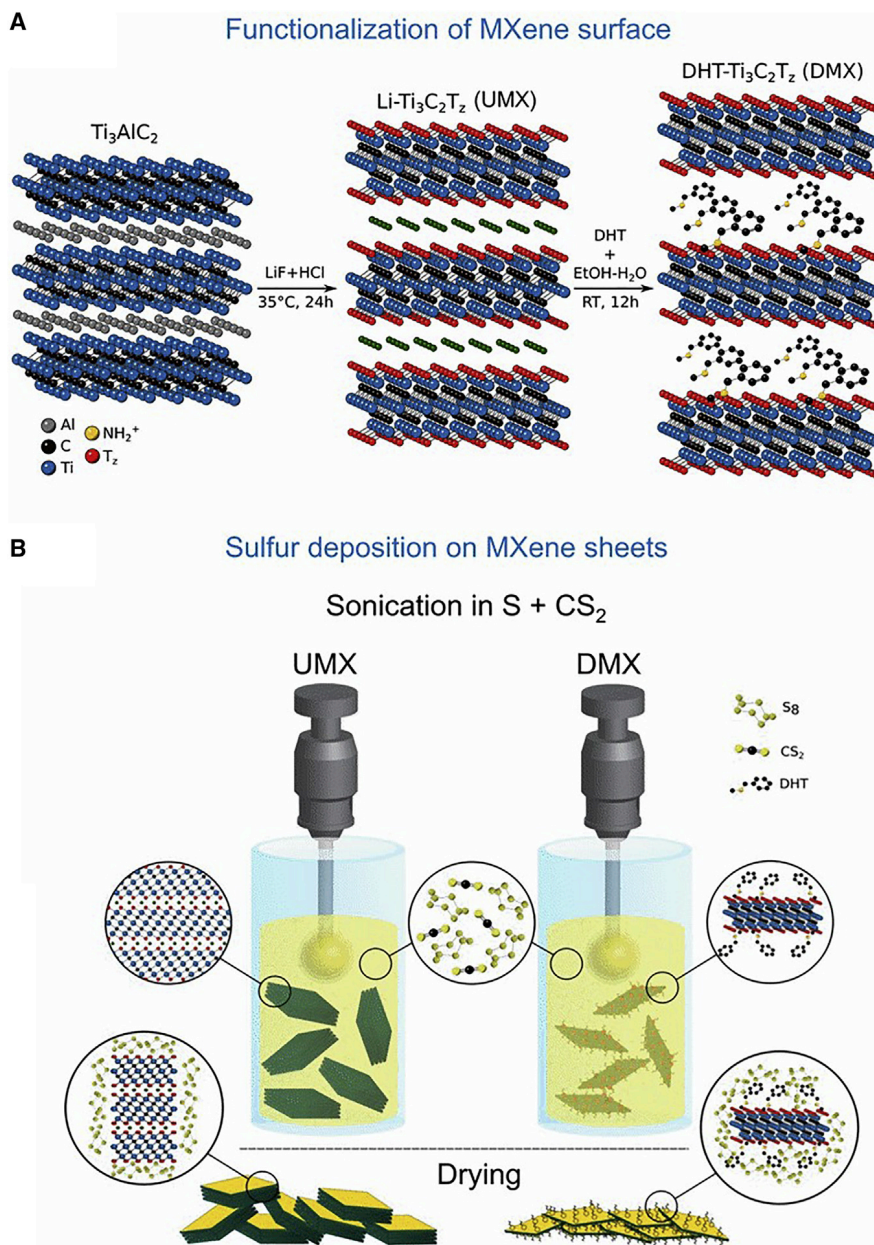


Figure 1. Surface treatment of MXene and formation of sulfur composite

(A) Schematic illustration of the etching Ti_3AlC_2 phase to yield UMX and the subsequent functionalization using DHT to yield DMX

(B) Fabrication procedure of MXene and sulfur composites (UMX/S and DMX/S) using probe ultrasonication and drying.

LiPs and MXene nanosheets. In addition, *ex situ* X-ray diffraction (XRD) and scanning electron microscopy (SEM) results demonstrate phase stability and better deposition of the active material, respectively, further strengthening our hypothesis.

RESULTS AND DISCUSSION

Material characterization

A schematic for the preparation of MXene from the parent Ti_3AlC_2 phase and its subsequent functionalization using DHT are shown in Figure 1A. The MXene etched

using LiF and HCl results in the intercalation of Li^+ ions between the MXene layers.⁴⁰ When the Li-containing multilayers (MLs) are exposed to DHT, they are replaced with DHT molecules via ion exchange.³⁰ The DHT-treated MXenes and untreated MXenes will be referred to as DMX and UMX, respectively.

Figure S1 shows the dispersion stability of untreated and DHT-treated MXenes in a non-polar organic solvent, carbon disulfide (CS_2). CS_2 is chosen because it is known to be a good solvent with high S solubility at room temperature (RT).⁴¹ The dispersions were made by probe sonicating both MXenes in CS_2 for 15 min under an ice bath. The colloidal suspensions were then allowed to sit and be monitored. The UMX sheets started to settle down within 30 s, as evidenced by the CS_2 starting to become transparent and clear. Meanwhile, the DHT-MXene suspension was stable even after 90 d. That stability is attributed to the organophilic nature of DMX, as long alkyl chains of DHT enhance the chemical stability in the non-polar CS_2 solvent.^{26,30} To confirm whether the addition of S would alter the stability, UMX and DMX flakes were sonicated in saturated S- CS_2 solutions (Figure S1). Here, again, the former sheets readily settled, whereas the latter were quite stable. Figure 1B depicts the fabrication strategy of MXene (UMX and DMX) and the sulfur composites. Typically, known quantities of sulfur and MXene (UMX and DMX) were probe sonicated in CS_2 , and then CS_2 was evaporated and dried using inert gas to yield UMX/S and DMX/S composites.

SEM micrographs of as-synthesized UMX (Figures S2A and S2B) and DMX (Figures S2C and S2D) powders before sonication in CS_2 show that both have a stacked ML structure. Further, SEM micrographs of the UMX/S powders (Figures 2A and 2B), recovered after the evaporation of CS_2 , display ML morphologies, confirming negligible delamination. On the other hand, SEM images of DMX/S powders show single to few-layer sheets with clear evidence of delamination (Figures 2D and 2E). To understand sulfur deposition throughout the DMX, we mapped the S-distribution with energy-dispersive X-ray spectroscopy (EDS). Figures 2C and 2F show the EDS maps of UMX/S and DMX/S, respectively. In the UMX/S case, S is found in regions in which no elemental Ti was detected. Conversely, in the DMX/S case, the Ti and S maps coincide, suggesting a uniform deposition of S onto the surface of the DMX sheets.

To further characterize the dispersion and deposition of S on the MXene surfaces, we drop casted and dried suspensions of UMX/S and DMX/S on a carbon-coated, copper grid and imaged the samples with transmission electron microscopy (TEM). Typical TEM images of UMX/S (Figure S3) show only nanosheets with little to negligible S deposition on the surface. It should also be noted that, because the UMX MLs do not delaminate in CS_2 , they are not electron transparent; because of which, finding areas in the sample with appropriate magnification for imaging is difficult. This was also observed in SEM-EDS mapping on the bulk scale (Figure 2C). On the other hand, TEM images (Figures 3A and 3B) of the DMX/S composite confirm the surface deposition of S on mostly single nanosheets. The selected area electron diffraction (SAED) patterns of DMX/S samples confirm the presence of diffuse rings in addition to the hexagonal $\text{Ti}_3\text{C}_2\text{T}_z$ crystal structure. These rings are most probably due to the presence of polycrystalline S. To further confirm S deposition, we performed high-resolution TEM analysis with a fast Fourier transform (FFT) filter to analyze the fringe distances. Figure 3D shows a fringe distance of 0.204 nm corresponding to orthorhombic S, confirming the presence of S on the 2D DMX nanosheets. At this stage, it is reasonable to conclude that we obtained a uniform S deposition onto the MXene sheets upon CS_2 evaporation.

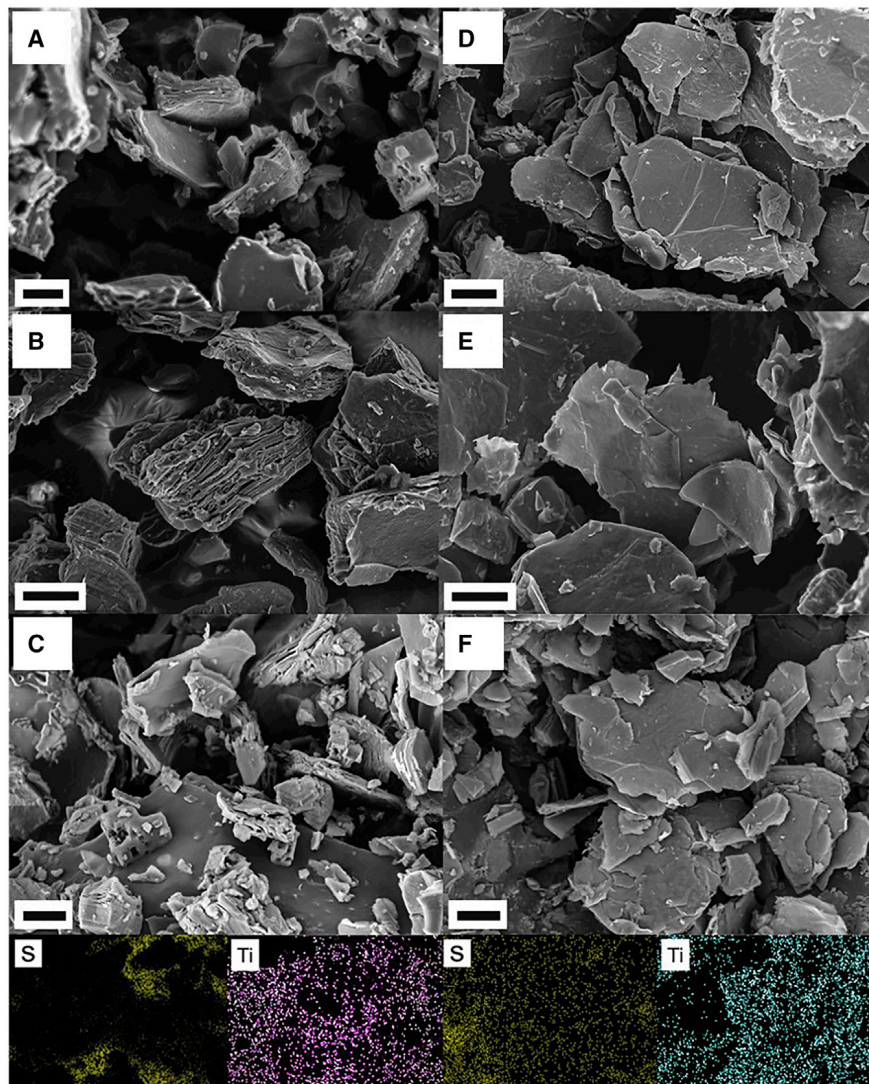


Figure 2. Electron microscopy images

(A and B) SEM micrographs of UMX/S.

(D and E) SEM micrographs of DMX/S.

(C and F) EDS images and mapping of UMX/S (C) and DMX/S (F).

Scale bar, 2 μm .

XRD patterns of DMX (blue), DMX/S (green), UMX (purple), and UMX/S (red) are compared in Figure 4A. The XRD pattern of pure S (black) is also plotted in Figure 4A. The presence of the (002) peak, around $6^\circ 2\theta$, corresponding to an interlayer spacing of 15 Å, is evidence for the presence of 2D MXene sheets.²⁶ Treating them with DHT, increases the d-spacing to 35 Å, confirming the successful exchange of Li^+ with DHT molecules.³⁰ After introducing the S, for both the DMX and UMX samples, a second 002 peak at a higher 2θ is observed, implying that some species were leached out of the interlayer space. The reason for that is unknown at this stage, and more work needs to be performed to understand this phenomenon. Overall, the DMX/S and UMX/S composites show the presence of S peaks in addition to the original MXene peaks, indicating no reaction between the MXene and S but physical mixing. No titanium dioxide peaks were observed, confirming that the nanolayers are non-oxidized. To quantify the amount of S in the DMX/S composite, thermogravimetric

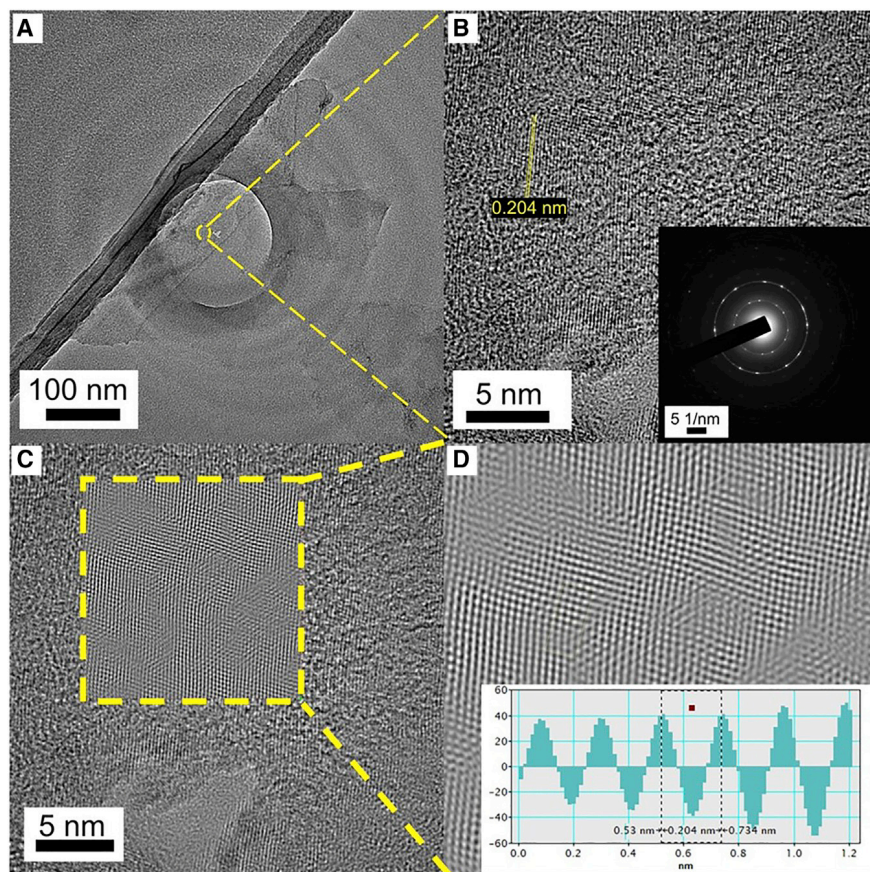


Figure 3. Surface analysis of MXene/S composite

(A) TEM micrograph of DMX/S.
(B) High-resolution TEM image of DMX/S (inset, SAED pattern of DMX/S).
(C and D) Interfringe distance analysis after FFT filter (D).

analysis (TGA) measurements were performed. A single-stage mass loss event in the 120°C–250°C temperature range was observed, which is due to S evaporation (Figure 4B). The content of the S was determined to be ~53 wt%.

Electrochemical characterization

The electrochemical performance evaluation of DMX/S cathodes were examined in coin-cell and pouch-cell configurations. The redox behavior was first evaluated by cyclic voltammetry and galvanostatic charge-discharge tests. The sulfur loading was varied between 1.8 mg·cm⁻² to 10.68 mg·cm⁻² for coin cells, and the capacity was calculated based on the mass of sulfur. To be able to compare the performances of the various electrodes, the electrolyte-to-sulfur ratio (mL·g⁻¹) in all coin cells was kept constant at 20. Figure 5A displays cyclic voltammograms (CVs) for DMX/S and UMX/S electrodes in the 1.8–2.6 V (versus Li/Li⁺) range at a scan rate of 0.1 mV·s⁻¹. The CV curves of the former show two sharp and distinct cathodic peaks and one anodic peak. The first cathodic peak, at 2.3 V, is ascribed to S reduction (S₈) to long-chain LiPs, whereas the second peak is related to a subsequent reduction of LiPs to Li₂S₂/Li₂S.⁴² Figure S4 shows the first five cycles of DMX/S, displaying almost no peak shifts after the first anodic cycle, indicating good electrochemical stability and better active material use. The peak shifts after the first anodic peak might be attributed to nucleation/reorganization during the redeposition of LiPs back to S₈. Meanwhile, the CV curves of the UMX/S electrodes

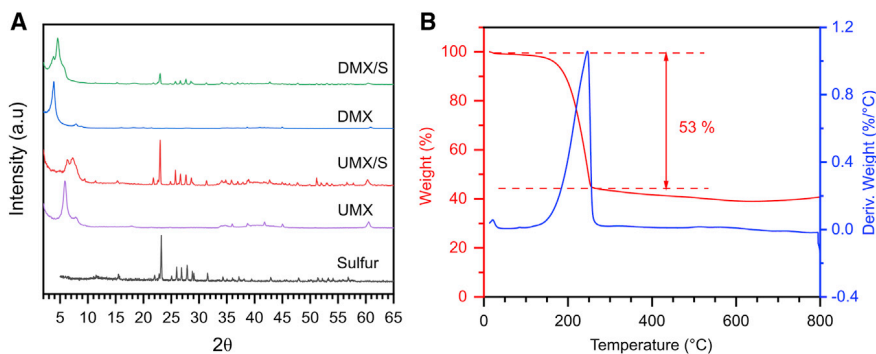


Figure 4. X-Ray diffraction and sulfur content analysis of MXene/S composites

(A) XRD patterns of UMX, DMX, sulfur, and its composites.

(B) TGA curve of DMX/S.

display a similar peak pattern, with broader and slightly shifted anodic and cathodic peaks. This can be attributed to an overpotential for the redox reaction to occur, most likely because of poor connectivity of S with the MXene nanosheets. Furthermore, the second cathodic peak has a lower contribution, denoting a low nucleating site for the deposition of $\text{Li}_2\text{S}_2/\text{Li}_2\text{S}$. The lower conversion characteristics might be attributed to the reduced active surface area of ML UMX compared with that of delaminated DMX.

Further, galvanostatic charge-discharge tests were performed at various current rates ($1\text{C} = 1,675 \text{ mA}\cdot\text{g}^{-1}$) for the DMX/S and UMX/S electrodes. Both display typical two-discharge plateaus. Consistent with the CV results, Figure 5B displays a higher-voltage plateau at 2.3 V and a lower one at 2.0 V, which we relate to the conversion of S to LiPs and LiPs to $\text{Li}_2\text{S}_2/\text{Li}_2\text{S}$, respectively (Figure 5A). Benefitting from the improved S-MXene interaction, DMX/S delivers an initial capacity of $\sim 1,300 \text{ mAh}\cdot\text{g}^{-1}$ compared with $\sim 605 \text{ mAh}\cdot\text{g}^{-1}$ from UMX/S. The lower initial-capacity form of the UMX/S composite might arise from the lower use of active materials, as seen from the prior CV curves. In addition, the polarization potential of the DMX/S electrodes has a smaller voltage gap of 0.28 V as compared with the 0.31 V of UMX/S (Figure 5B). Lower polarization potential is beneficial for better use of S at higher loadings because it correlates the kinetics of the charge transfer with the activation energies for the LiP conversion.⁴³ Hence, the lower polarization potential of DMX/S might indicate better electrocatalytic activity that enhances the kinetics during the conversion of LiPs. Similarly, Nyquist plots demonstrate the lower charge transfer resistance of DMX/S cathode compared with that of UMX/S, suggesting lower resistance to undergoing the reaction (Figure S5). This behavior is probably associated with improved local conductivity from delaminated MXene sheets coupled with the use of higher functionally active groups on the DMX nanosheet compared with that of the UMX.

To evaluate the long-term stability, DMX/S and UMX/S electrodes were cycled at 0.5C, as shown in Figure 5C. As noted above, the former delivers a high initial capacity of $\sim 1,300 \text{ mAh}\cdot\text{g}^{-1}$, which stabilizes to $\sim 900 \text{ mAh}\cdot\text{g}^{-1}$ after the first five cycles. This initial drop is associated with the redistribution of S in the electrode during the first few electrochemical cycles. Once the cathode stabilizes, it delivers a high specific capacity of ~ 860 , ~ 850 , ~ 800 , ~ 780 , and $\sim 750 \text{ mAh}\cdot\text{g}^{-1}$ after 100, 200, 300, 400, and 500 cycles, respectively. In other words, the electrode retains around $750 \text{ mAh}\cdot\text{g}^{-1}$, accounting for $\sim 85\%$ of its initial stable capacity after 500 cycles with a 0.003% decay rate per cycle. The above results indicate that DMX/S can

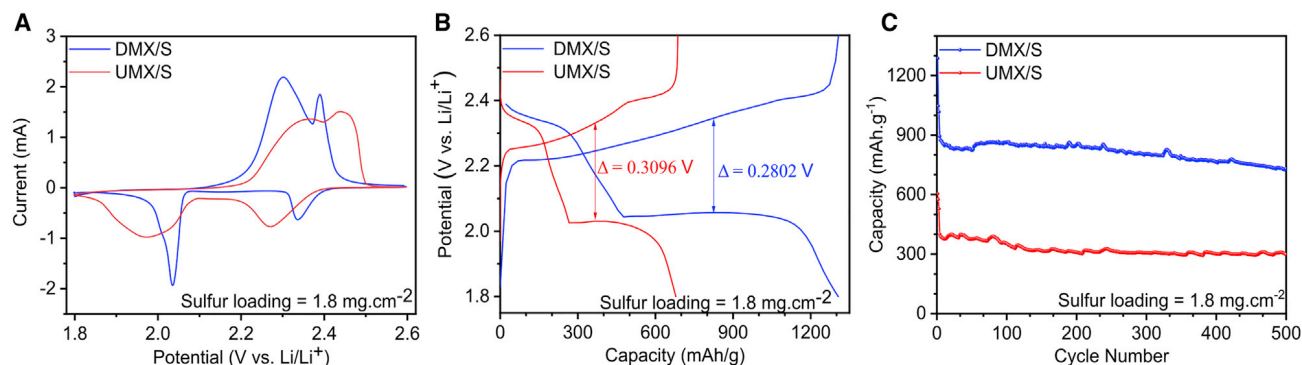


Figure 5. Electrochemical analysis of DMX/S and UMX/S

(A) Comparison between CV curves of DMX/S and UMX/S.

(B) Charge-discharge curves of DMX/S and UMX/S.

(C) Cycling stability curves at 0.5C of DMX/S and UMX/S.

efficiently use the active material because of their improved delaminated structure and possibly bind LiPs effectively, thereby enhancing capacity and cycling stability.

Meanwhile, the UMX/S electrode delivers an initial capacity of $\sim 605 \text{ mAh}\cdot\text{g}^{-1}$, which stabilizes to $\sim 350 \text{ mAh}\cdot\text{g}^{-1}$ after the first five cycles and then remains stable at $300 \text{ mAh}\cdot\text{g}^{-1}$ after 500 cycles. This lower capacity can be attributed to a lower active electrochemical area, which is unable to use S efficiently during the redox reactions. Furthermore, the formed LiPs are probably repelled by the hydrophilic UMX sheets, enhancing the shuttling and reducing the blocking of LiPs. Because the $\text{Ti}_3\text{C}_2\text{T}_z$ sheets are expected to bind to LiPs via polar-polar and Lewis-acid-base interactions, the active surface area of DMX/S is significantly larger than that of UMX/S, possibly because of improved delamination, improving the capacity of the former but keeping cycling stability similar. Figure S4B shows the discharge capacity of DMX/S electrodes at various current rates. The high capacities of 1,380, 1,250, 850, and $780 \text{ mAh}\cdot\text{g}^{-1}$ at 0.05, 0.1, 0.2, and 1C, respectively, were obtained.

High current cycling is one of the key parameters for most batteries, in general, and for Li-S batteries, in particular. To evaluate those parameters for the DMX/S electrodes, we performed a galvanostatic charge-discharge test at a relatively high rate of 1C. At that rate, the electrode initial capacity was $\sim 1,100 \text{ mAh}\cdot\text{g}^{-1}$, which stabilized to $720 \text{ mAh}\cdot\text{g}^{-1}$ after five cycles (Figure 6A). The electrode delivered ~ 700 , 600, and $450 \text{ mAh}\cdot\text{g}^{-1}$ after 250, 500, and 1,000 cycles, thus retaining $\sim 97\%$, 85%, and 62% of its initial capacity, respectively. Figure 6B shows the rate capability evaluated at various current rates. The successive current increment from 0.1, 0.2, 0.5, and 1C for five cycles delivers a stable capacity of $\sim 1,000$, ~ 850 , ~ 780 , and $\sim 700 \text{ mAh}\cdot\text{g}^{-1}$, respectively. When the current rates were returned to 0.1C and 0.5C, the cathode recovered back the capacity, delivering $\sim 1,000$ and $\sim 770 \text{ mAh}\cdot\text{g}^{-1}$, respectively. Although the overpotentials between the charge-discharge curves increased with the improvement in the current rate, they all demonstrated the two-plateau behavior, indicating stability and use at different current rates.

To explore the effect of S-loading, we performed the galvanostatic charge-discharge test at 0.5C at loadings $> 5 \text{ mg}\cdot\text{cm}^{-2}$. The initial capacity is reduced to $1,000 \text{ mAh}\cdot\text{g}^{-1}$ for $5.5 \text{ mg}\cdot\text{cm}^{-2}$ compared with $1,300 \text{ mAh}\cdot\text{g}^{-1}$ at $1.8 \text{ mg}\cdot\text{cm}^{-2}$ at a current rate of 0.5C (Figure 6C). These high-loading cathodes deliver a stable capacity of $\sim 500 \text{ mAh}\cdot\text{g}^{-1}$ after 250 cycles (Figure 6C). This cycling performance

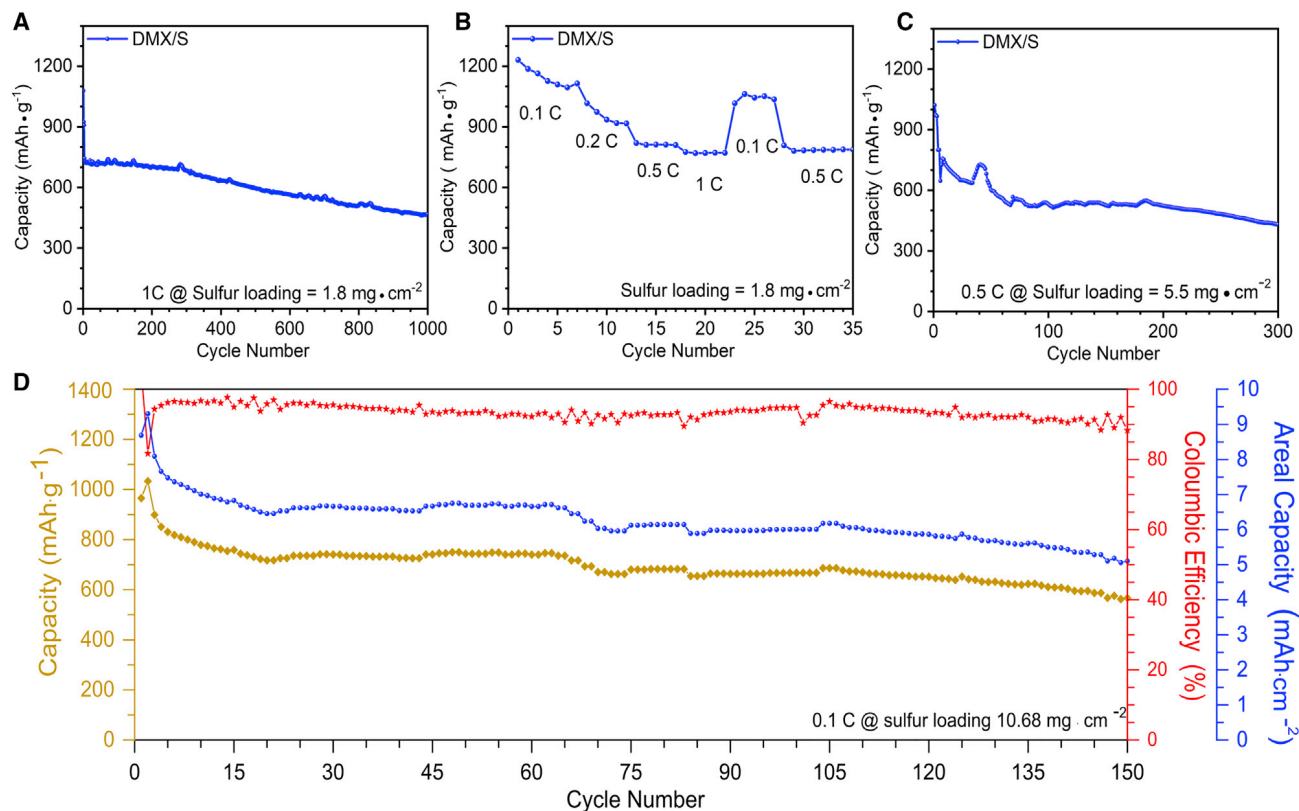


Figure 6. High sulfur loading and rate analysis

(A) Cycling stability curve of DMX/S at 1C.

(B) Rate characteristics of DMX/S.

(C) Cycling stability curve at high loading and moderate current rate of 5.5 mg·cm⁻² at 0.5C.

(D) Cycling performance of DMX/S cathode at high loading of 10.68 mg·cm⁻².

at such high mass loadings with a high C-rate is noteworthy. This response can be related to the combined effects of better use of the active material; increased nucleating sites for LiPs deposition; more LiPs trapping sites, mitigating the shuttle effects; and the metallic conductivity of Ti₃C₂T_z nanosheets, allowing for efficient electron transfer during the redox reactions.

To observe the effect of shuttling in the DMX/S electrode, we conducted a charge-discharge test at the harsh low-current rate of 0.1C, with a high loading of 10.7 mg·cm⁻² (Figure 6D). This low current increases the time for LiP shuttling and can be used as an indirect measure of the binding effect of the DMX/S electrodes with the LiPs. The initial capacity was 925 mAh·g⁻¹ (9.25 mAh·cm⁻²), which stabilizes (~800 mAh·g⁻¹) and delivers ~600 mAh·g⁻¹ after 150 cycles, still retaining 75% of the stabilized capacity (Figure 6D). This result indicates an improvement in use at high S loadings and delivers stable capacity. This performance enhancement can be attributed to better use of the MXene nanosheet surface for efficiently binding LiPs and faster conversion/reduction of the same, helping to extend the cycle life.

Along the same lines, the next-generation high-energy-density Li-S cells will require higher weight loadings of active material to improve the areal capacity. Hence, DHT/S cathodes were fabricated with 83% mass S loading, henceforth, referred to as DMX/83S. Figure S6 shows the discharge profile of cathodes at a 2.4 mg·cm⁻² loading. The composite displays the two-plateau discharge behavior with slightly

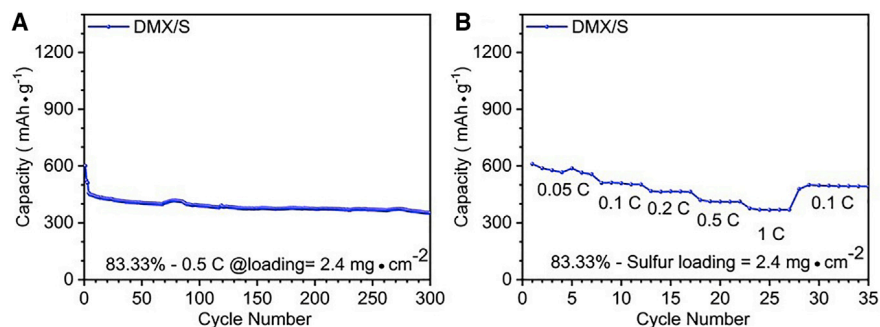


Figure 7. Electrochemical analysis of high-sulfur-weight-percentage cathodes

(A) Cycling stability at 83.33% loading with $2.4 \text{ mg} \cdot \text{cm}^{-2}$ sulfur loading at 0.5C.

(B) Rate characteristics of DMX/S at 83.33% sulfur loading.

greater polarization compared with prior tests (Figure S6). The greater polarization potential indicates reduced composite conductivity because of improvement in insulating the sulfur content, increasing the voltage for a redox reaction. Overall, the DMX/83S electrode delivers a capacity of $450 \text{ mAh} \cdot \text{g}^{-1}$ after five cycles and 80% of its initial capacity ($\sim 400 \text{ mAh} \cdot \text{g}^{-1}$) after 300 cycles, (Figure 7A). Figure 7B plots the rate capability of the DMX/83S electrode that delivers a capacity of 580, 520, 430, and $380 \text{ mAh} \cdot \text{g}^{-1}$ at 0.05, 0.1, 0.2, 0.5, and 1C, respectively. When the current is decreased back to 0.1C, the capacity rebounds to $\sim 515 \text{ mAh} \cdot \text{g}^{-1}$. This performance at high S loading and with high S wt% (83 wt%) should be ascribed to the convoluted effect of the highly active surface area of the conductive, delaminated DMX sheets and their LiP-trapping ability. It is important to note, the sulfur wt% loading is the highest reported in MXene/S literature, further suggesting the importance of the host-sulfur architecture in the use of the active material.

Finally, to evaluate the practicality of using DMX/S as cathodes, we assembled pouch cells. Single-layer pouch cells were assembled with DMX/S as the cathode, Li metal foil ($\sim 200 \mu\text{m}$) as an anode, and a Celgard separator, inside a glove box (Figure 8A). The assembly was then sealed in a laminated Al pouch (thickness = $110 \mu\text{m}$) inside the glove box using a 3-in-1 vacuum pouch sealer. The pouch cell with a sulfur loading of 60 mg was evaluated with a similar E/S ratio as that of the coin cell. The pouch cell demonstrated an initial capacity of $1,200 \text{ mAh} \cdot \text{g}^{-1}$ (0.05C), which stabilized to $900 \text{ mAh} \cdot \text{g}^{-1}$ after five cycles at 0.2C. The capacity after 50, 100, and 190 cycles were 892, 890, and $770 \text{ mAh} \cdot \text{g}^{-1}$ (Figure 8C), demonstrating capacity retentions of 99%, 98% and 85.5%, respectively. Figure 8B shows the charge-discharge behavior of the pouch cells after various cycle numbers. The overlapping discharge profiles indicate better S use during the entire cycle life and minimal shuttling, even at electrode areas of $5 \times 5 \text{ cm}^2$ (Figure 8A), showing a potential for practical applications. Figure S7 shows the cycling performance of the pouch cell at a low sulfur loading of 11 mg delivering 840, 700, and $654 \text{ mAh} \cdot \text{g}^{-1}$ after 50, 200, and 400 cycles, respectively. The purpose of this study was to evaluate the performance of the cathodes with increased geometrical area, thereby keeping other parameters similar to that of the coin-cell testing. Evaluation of pouch cells with optimized E/S ratios and improved sulfur loading will be the focus of our future work. The key takeaway from the pouch results is that scaling our system did not in any way invalidate our excellent results. This bodes very well for scaling up our technology and cannot be overemphasized.

Figure 9 compares our work with other MXene/S composite hosts reported in literature. It correlates deliverable capacity of the hosts at various areal sulfur loadings

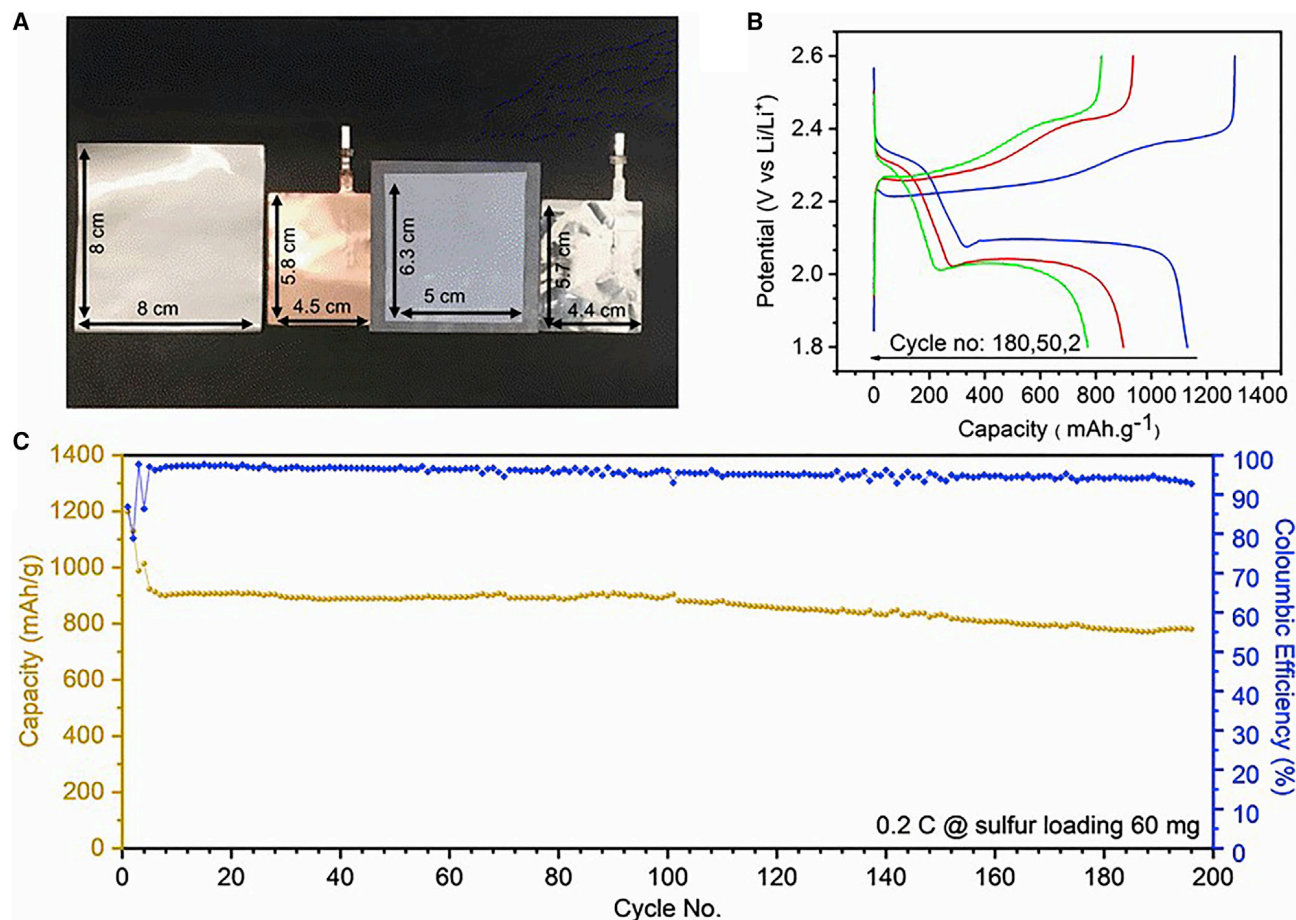


Figure 8. Pouch-cell-level performance

(A) Single-layer pouch-cell assembly parts (laminated pouch, copper current collector welded with a nickel tab, Celgard 2325 separator, and aluminum current collector welded with an aluminum tab).

(B) Charge-discharge curves of DMX/S after various cycles at 60 mg S loading.

(C) Cycling stability of the DMX/S pouch cell.

(1–12 mg · cm⁻²) and current rates (0.5, 0.2, and 0.1C). To our knowledge, we are the first to report a surface-functionalized MXene, DMX/S, composite cathode enabling a high sulfur use of 10.7 mg · cm⁻² at a current rate of 0.1C with cycling stability for 150 cycles. In addition, DMX/S cathode (navy blue star) outperforms the other MXene hosts reported in the literature in all three regimes of sulfur loadings, current rates with improved cycling stability, and higher capacity. Such improvement in performance, high specific capacity, good cycling stability, and use of sulfur at high loadings can be attributed to (1) the metallic sheet conductivity of MXenes in DMX/S composites; (2) greater use of individual sheet-surface area, rendering better use of sulfur; and (3) improved accessibility of functional groups and LiP trapping sites, enabling possible Lewis-acid-base interactions. Therefore, DMX/S cathodes bestow better advantages compared with the other Ti₃C₂T_z-MXene hosts reported in the literature, thereby demonstrating better performance metrics.

Redox kinetics of LiPs on DMX surfaces

The Li-ion diffusion coefficients can be used to estimate the relative concentration of LiPs in the electrolyte. A lower concentration of LiPs in the electrolyte results in faster Li-ion diffusion and vice versa.⁴⁶ To investigate the Li-ion diffusion kinetics, CVs, at

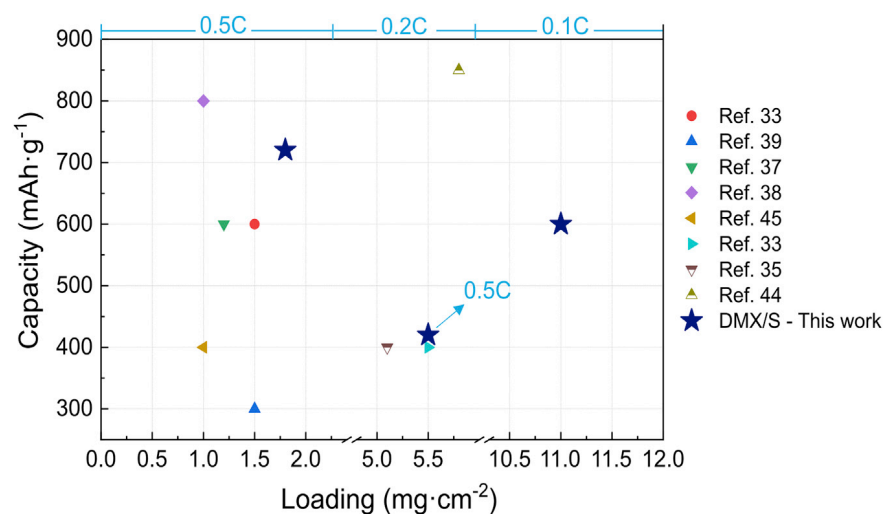


Figure 9. Performance compared with literature articles

Comparison of capacity versus areal sulfur-loading characteristics at various current rates of DMX/S with MXene hosts in the literature. A star (navy blue) indicates the capacity of DMX/S cathodes at various sulfur loadings and current rates.^{33,35,37,38,39,44,45}

scan rates ranging from $0.1 \text{ mV} \cdot \text{s}^{-1}$ to $0.5 \text{ mV} \cdot \text{s}^{-1}$ between 1.8 V and 2.6 V versus Li/Li⁺, were obtained (Figures 10A and 10B). The cathodic and anodic current peaks (labeled a, b, and c in Figures 10A and 10B) of the DMX/S and UMX/S electrodes scale linearly with the square root of the scan rates as shown in Figures 10C and 10D. This indicates a diffusion-limited process.

As reported previously, the Li-ion diffusion process can be described by the Randles-Sevcik equation,^{46–50} given by Equation 1:

$$I_p = (2.69 \times 10^5) n^{1.5} A D_{\text{Li}}^{0.5} C_{\text{Li}} \nu^{0.5} \quad (\text{Equation 1})$$

where I_p is the peak current (A), n is the charge transfer number, A is the active electrode area (cm^2), D_{Li} is the lithium-ion diffusion coefficient ($\text{cm}^2 \cdot \text{s}^{-1}$), C is the concentration of Li ions ($\text{mol} \cdot \text{cm}^{-3}$), and ν is the scan rate ($\text{V} \cdot \text{s}^{-1}$). Because the n , A , and C in a given cell can be regarded as constants, the slope of I_p versus $\nu^{0.5}$ plots are proportional to D_{Li} . Figure S8 shows that the UMX/S and DMX/S electrodes exhibit similar D_{Li} values in the “a” region, where the S to LiPs conversion occurs. However, as shown in Figures 10C and 10D, we see a striking difference in the conversion of LiPs to Li₂S and LiPs back to S. We see low Li diffusion for UMX/S compared with DMX/S. Such behavior might arise from lower nucleating sites for LiPs on the hydrophilic UMX surface. Meanwhile, the hydrophobic surface of DMX/S might contribute toward better deposition, which results in further improved current response, as seen from CV curves.

Postmortem studies

Finally, to fundamentally understand the nature of the interactions exhibited between LiPs and Ti₃C₂T_z, we performed postmortem X-ray photoelectron spectroscopy (XPS) analysis. The Li-S cells were stopped after completely discharging after 500 cycles at 0.5C. The cycled cells were de-crimped inside the Ar-filled glove box and were transferred to the XPS chamber using an Ar-purged XPS assembly. For reference, we conducted similar experiments on a normal UMX/S-cycled cathode. Note S1 goes into detail about the XPS analysis. Simultaneously, we performed

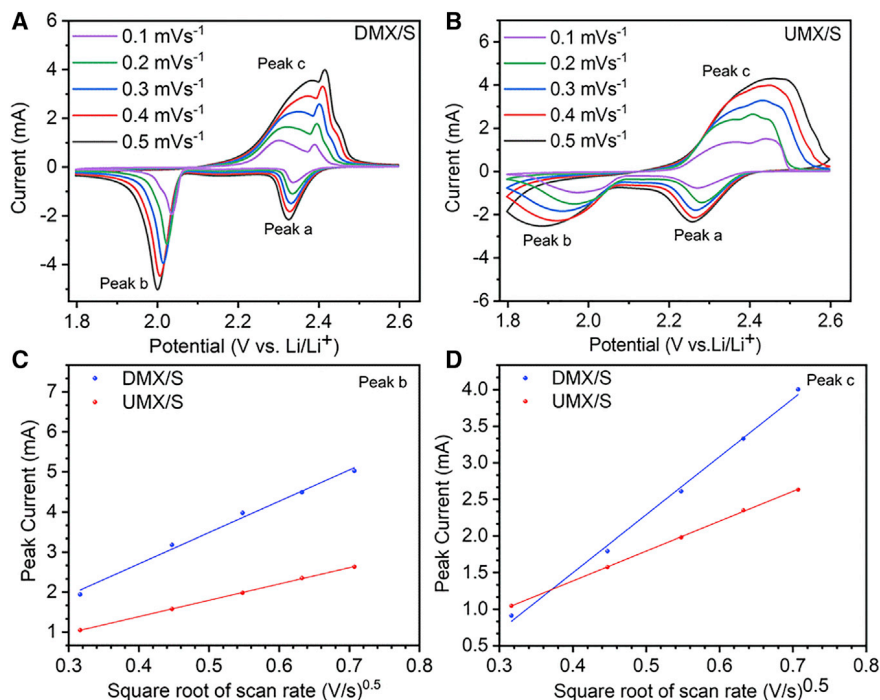


Figure 10. Li⁺ ion diffusion study

(A and B) CV curves of DMX/S and UMX/S at various scan rates

(C and D) The relationships between the peak current and scan rate for different reaction processes in the DMX/S and UMX/S composites. Peak b: $\text{Li}_2\text{Sx} \rightarrow \text{Li}_2\text{S}_2/\text{Li}_2\text{S}$ (c); peak c: $\text{Li}_2\text{Sx} \rightarrow \text{S}_8$ ($4 \leq 8$) (d).

postmortem SEM and XRD analysis to evaluate the surface morphology and stability of MXenes in the system after cycling.

Figure S9 shows postmortem XRD results for the cycled cathodes (DMX/S and UMX/S) after discharge. In the XRD pattern of the cycled UMX/S and DMX/S cathodes, the presence of the (002) peak around $6^\circ 2\theta$ ($d = 15 \text{ \AA}$) confirms the presence of 2D MXene sheets. This suggests the formed Lewis-acid-base Ti-S bond is reversible and does not hamper MXene structure, enabling it to continue binding LiPs. However, because the electrode was disassembled in a completely discharged state and was exposed to air during XRD measurements, the Li_2S being air sensitive might have converted to H_2S and amorphous LiOH , demonstrating no peak pattern.⁵¹

Finally, to understand the effect of cycling on the MXene cathodes, we performed SEM analysis on DMX/S and UMX/S cathodes of cycled cells. Figures S10A and S10B shows sulfur is completely deposited on the surface and the outer surface of UMX supporting our initial hypothesis of this work. Simultaneously, in DMX/S cathodes (Figures S10C and S10D), we still see single to a few flakes of MXene nanosheets without aggregation, denoting good adherence of material and suggesting cycling does not have any effect on cathode morphology. Furthermore, EDS data of the cycled UMX/S cathode show negligible titanium signal compared with S (Figure S10E). This can be attributed to thick and non-uniform sulfur deposition on the surface of UMX/S. In contrast, in Figure S10F, we see orderly Ti and S signals from the DMX/S cathode because of the uniform deposition of sulfur by taking an advantage of numerous active area/nucleating sites on a few to a single DMX nanosheet.

In summary, we are developing a new and facile design strategy, in which $\text{Ti}_3\text{C}_2\text{T}_z$ nanosheets surfaces are engineered to fabricate S electrodes. The MXene surfaces are first modified using an inexpensive organic molecule, DHT, which results in easy dispersion of MXene sheets in S-dissolved CS_2 . Upon evaporation of the solvent, S conformally and uniformly deposits on the 2D layer surfaces. This method eliminates the use of the energy-extensive, high-temperature treatment method for S diffusion and results in efficient deposition of S on the MXene surface. In principle, the CS_2 used can be recycled after its evaporation, further reducing the synthesis cost. The DMX/S electrodes deliver a stable capacity of $\sim 750 \text{ mAh}\cdot\text{g}^{-1}$ after 500 cycles at 0.5 C, retaining $\sim 85\%$ capacity after the first five cycles. Furthermore, at a high current rate of 1C, the cathode delivers an initial capacity of $\sim 720 \text{ mAh}\cdot\text{g}^{-1}$ and retains $\sim 80\%$ of its capacity after 500 cycles. The electrode can also operate at a high loading of $10.7 \text{ mg}\cdot\text{cm}^{-2}$, with an initial areal capacity of $\sim 8 \text{ mAh}\cdot\text{cm}^{-2}$ and a stable capacity of $\sim 600 \text{ mAh}\cdot\text{g}^{-1}$ for 150 cycles. In addition, the electrode is operational at high weight loading, with 83.33 wt% of the sulfur retaining stability after 300 cycles at 0.5C. A single-layer pouch cell successfully demonstrates a high sulfur loading of 60 mg, delivering $\sim 770 \text{ mAh}\cdot\text{g}^{-1}$ (85.5% retention) after ~ 200 cycles. This cathode outweighs performance characteristics in all current and sulfur-loading regimes compared with other MXene/S hosts in literature. Postmortem XPS studies reveal the presence of strong Lewis-acid-base bonds (Ti-S) between the DMX/S and LiPs. In addition, the XPS study also reveals the presence of thiosulfate/polythionate complex formation. We attribute the strong electrochemical performance to the unique electrode design, coupled with the metal-like conductivity of the $\text{Ti}_3\text{C}_2\text{T}_z$ flakes. Our design strategy paves a new path for the development of Li-S batteries with high loading and long cycle life.

EXPERIMENTAL PROCEDURES

Resource availability

Lead contact

Further information and requests for resources and reagents should be directed to, and will be fulfilled by, the lead contact, Vibha Kalra (vk99@drexel.edu)

Materials availability

All MXenes and composites generated in this study are available from the lead contact with a completed materials-transfer agreement.

Data and code availability

All of the data are available from the corresponding author upon request.

Material for synthesis

Titanium carbide (TiC; 99.5%, 2 μm), aluminum (Al; 99.5%, 325 mesh), titanium (Ti; 99.5%, 325 mesh), and LiF (99.5%, 325 mesh) were purchased from Alfa Aesar. The 12-M HCl was purchased from Fisher Scientific and DHT (80%) was purchased from Alfa Chemistry.

Materials for electrochemistry

Lithium trifluoromethanesulfonate (99.995% trace metals basis, product no. 481548), 2-dimethoxyethane (DME; anhydrous, septum-sealed bottle DriSolv, product no. DX1531), and 1,3-dioxolane (DOL; anhydrous, contains ~ 75 ppm BHT as an inhibitor, 99.8%, SureSeal, product no. 271020) were purchased from Sigma-Aldrich. Sulfur (99.5%, sublimed, catalog no. AC201250025), carbon disulfide (reagent grade, catalog no. C184-500), and lithium nitrate (anhydrous, 99.98%, catalog no. AA1098503) were purchased from Fisher Scientific.

Synthesis of MAX powder (Ti_3AlC_2)

Parent Ti_3AlC_2 powders were synthesized by mixing TiC, Al, and Ti powders in a molar ratio of 2:1.05:1, respectively. The mixed powders were ball milled at 100 rpm for 24 h and were then heated under argon (Ar) flow at 1,350°C for 2 h. It should be noted that the ball milling at slow speed was only for homogeneous mixing; no particle size reduction or reactions occurred. The heating and cooling rates were set at 5°C/min. The resulting blocks were ground to powders using a milling bit on a drill press. The milled powders were passed through a 400-mesh (particle size, <38 μm) sieve for further experiments.

Synthesis of MXene ($\text{Ti}_3\text{C}_2\text{T}_2$) and DHT treatment

First, 1 g of LiF was dissolved in 10 mL of 12-M HCl; after which, 1 g of the Ti_3AlC_2 powder was slowly added to the solution. Then, the solution was stirred for 24 h at 35°C and 300 rpm. The resulting solution was later transferred into a 50-mL centrifuge tube, and deionized (DI) water was added to completely fill the remaining volume. It was then centrifuged at 3,500 rpm/2,300 relative centrifugal force (*rcf.*) for 1 min, and the resulting clear supernatant was discarded. This washing was repeated several times, until the pH of the solution was ≈ 7 . Afterward, the sediment was divided into two equal parts. One part was dried in vacuum at 100°C for 12 h and was labeled as normal, untreated MXene or UMX. In the second part, 40 mL of a 20-mM, pre-prepared solution of DHT in a 50:50 (v:v) of water and ethanol was added and allowed to mix for 12 h at RT. After mixing, all the powders were washed with DI water three times. The resulting DHT-MXene or DMX was dried in vacuum at 100°C for 12 h.

Synthesis of MXene-sulfur composite

Moderate-weight-percentage electrodes, 50 wt%

In a typical synthesis, 1 g of sulfur was added to 5 mL of CS_2 solution in a glass vial. The glass vial was kept in an ice bath, and the vial was hand-shaken until the sulfur dissolved and the solution turned clear. Next, 1 g of DHT-MXene (DMX) was added to that solution and was probe-sonicated (250 W) for 15 min in an ice bath. After probe-sonication, argon was slowly blown on top of this solution and magnetically stirred (320 rpm) until the CS_2 completely evaporated. Once the CS_2 had been visibly evaporated, the solid mixture was vacuum dried at RT for 12 h to yield the DMX/S powder. A similar strategy was employed for normal MXene (UMX/S).

High-weight-percentage electrodes, 83.33 wt%

A procedure similar to the low-weight-percentage electrodes was adopted; except, 5 g of sulfur was added to 20 mL of CS_2 solution with 1 g of MXenes.

Synthesis of DMX/S and UMX/S composite electrode

A cathode was fabricated using a slurry method. Briefly, the slurry was prepared by mixing 70 wt% of vacuum-dried DMX/S with 20 wt% conductive carbon (Alfa Aesar, Super P) and 10 wt% battery-grade polyvinylidene fluoride (PVDF) binder (MTI, USA). DMX/S, conductive carbon, and PVDF were hand-ground with mortar and pestle until the composite turned uniform. Later, *N*-methyl-2-pyrrolidone (TCI, USA) was slowly added until the required visible consistency and uniformity were achieved (~ 1 h). The slurry was later cast on battery-grade aluminum foil coated with 1- μm -thick conductive carbon for better adhesion using a doctor blade (MTI, USA), with a thickness of 30–120 μm . To improve sulfur loading, the thickness of the slurry was increased by the changing dial gauges of the doctor blade. Once cast, the slurry was kept under a closed fume hood for 2 h before transferring it to a vacuum oven, where it was dried at 50°C for 24 h.

Material characterization

The morphological analysis of the materials was conducted using an SEM (Zeiss Supra 50VP, Germany) with an in-lens detector, and a 30-mm aperture was used to examine the morphology and to obtain micrographs of the samples. To analyze the surface elemental composition, EDS (Oxford Instruments) in secondary electron-detection mode was used. To analyze the sulfur deposition on the surface, TEM measurements were conducted. High-resolution transmission electron microscope (HR-TEM) analyses were performed in brightfield mode, operated at 200 kV on a JEOL JEM2100F equipped with an energy-dispersive spectroscopy (EDS), with an 80-mm² single-shot detector (Oxford X-MaxN 80 T EDS system). XRD patterns were acquired on a diffractometer (Rigaku Miniflex, Tokyo, Japan) using Cu-K α radiation (40 kV and 40 mA), with a step size of 0.02° and a dwell time of 5 s, in the 2°–65° 2 θ range. The surface of the composites was analyzed with XPS. To collect XPS spectra, Al-K α X-rays, with spot sizes of 200 μ m and pass energy of 23.5 eV were used to irradiate the sample surface. A step size of 0.05 eV was used to gather the high-resolution spectra. CasaXPS (version 23.19PR1.0) software was used for spectra analyses. The XPS spectra were calibrated by setting the valence edge to zero, which was calculated by fitting the valence edge with a step-down function and setting the intersection to 0 eV. The background was determined using the Shirley algorithm, which is a built-in function in the CasaXPS software. The sulfur in the composite was determined using TGA on a TA Instruments Q50. The samples were heated at a ramp rate of 10°C·min⁻¹ to 800°C under flowing argon gas.

Coin-cell fabrication

The dried electrodes were cut using a hole punch (ϕ = 0.5 inch [12.7 mm]) to form disk-sized electrodes. The electrodes were then weighed and transferred to an argon-filled glove box (MBraun LABstar, O₂ < 1 ppm and H₂O < 1 ppm). The CR2032 (MTI and Xiamen TMAX Battery Equipments, China) coin-type Li-S cells were assembled using DMX/S and UMX/S (ϕ = 12 mm), lithium disk anodes (Xiamen TMAX Battery Equipment's; ϕ = 15.6 mm, 450 μ m thick), a tri-layer separator (Celgard 2325; ϕ = 19 mm), one stainless-steel spring, and two spacers, along with an electrolyte. The electrolyte with 1-M LiTFSi with 1 wt% LiNO₃ in a mixture of 1,2-dimethoxyethane and 1,3-dioxolane at a 1:1 volume ratio was purchased from TMAX Battery Equipments, with H₂O < 6 ppm and O₂ < 1 ppm. The assembled coin cells were rested at their open-circuit potential for 12 h to equilibrate them before performing electrochemical experiments at RT. Cyclic voltammetry was performed at various scan rates (0.1 mV·s⁻¹ to 0.5 mV·s⁻¹) between voltages 1.8 and 2.6 V wrt Li/Li⁺ with a potentiostat (Biologic VMP3). Prolonged cyclic stability tests were carried out with a MACCOR (4000 series) and Neware BTS 4000 battery cycler at different C-rates (where 1C = 1,675 mAh·g⁻¹) between voltages 1.8 and 2.6 V. Li-S cells were conditioned during the first cycle at the 0.1C and during the second cycle at the 0.2C rate before cycling them at the 0.5C rate at RT.

Pouch-cell fabrication

Cathodes were punched with dimensions 57 mm × 44 mm using MSK-T-11 (MTI, USA). A 4-inch (101.6 mm) lithium strip (750 μ m, Alfa Aesar) was rolled in between aluminum-laminated film to get a 60 mm × 50 mm Li sheet using an electric hot-rolling press (TMAX-JS) at 0.328 rpm inside the glove box (MBraun, LABstar Pro). Once the final dimensions of lithium were achieved (~200–250 μ m thick), it was re-rolled with copper (10 μ m) to achieve good adhesion. Finally, the lithium-rolled copper sheet was punched with a 58-mm × 45-mm die cutter (MST-T-11) inside the glove box. The cathode and anode were welded with aluminum and nickel tabs (3 mm), respectively. The tabs were welded with an 800-W ultrasonic metal welder, with

40 KHz frequency; delay time of 0.2 s, welding time of 0.15 and 0.45 s for Al|Al and Cu|Ni, respectively; and cooling time of 0.2 s with 70% amplitude. The anode and cathode were placed between a Celgard 2325 separator, and the pouch was sealed with 3-in-1 heat pouch sealer inside the glove box with a -95 kPa vacuum, 4-s sealing time at 180°C and a 6-s degas time.

SUPPLEMENTAL INFORMATION

Supplemental information can be found online at <https://doi.org/10.1016/j.xcrp.2021.100480>.

ACKNOWLEDGMENTS

The authors would like to thank the National Science Foundation (CMMI- 1804374, 1919177, and DMR-1740795). We are especially thankful to the MCC facility at Drexel University for help with materials characterization equipment. We would also like to thank Mengwen Yu from Dr. Giuseppe Palmese's group for her help with the thermogravimetric analysis.

AUTHOR CONTRIBUTIONS

R.P., V.N., M.W.B., and V.K. designed and executed the study. R.P. performed all the electrochemical experiments and wrote the manuscript. M.C. and V.N. performed the synthesis and functionalization of MXenes. V.N. assisted in the SEM and XPS measurements and analyzed the XPS data. M.S. performed all TEM measurements and analyzed and put together the data. All authors contributed to the editing of the manuscript, and M.W.B. and V.K. supervised the project.

DECLARATION OF INTERESTS

A patent has been filed for the above work under the title "Dispersion and stabilization of MXene materials and MXene materials for energy storage applications." The authors declare no other competing interests.

Received: March 10, 2021

Revised: April 23, 2021

Accepted: June 4, 2021

Published: June 29, 2021

REFERENCES

- Armand, M., and Tarascon, J.M. (2008). Building better batteries. *Nature* 451, 652–657.
- Manthiram, A., Fu, Y., Chung, S.H., Zu, C., and Su, Y.S. (2014). Rechargeable lithium-sulfur batteries. *Chem. Rev.* 114, 11751–11787.
- Bruce, P.G., Freunberger, S.A., Hardwick, L.J., and Tarascon, J.M. (2011). Li-O₂ and Li-S batteries with high energy storage. *Nat. Mater.* 11, 19–29.
- Yin, Y.X., Xin, S., Guo, Y.G., and Wan, L.J. (2013). Lithium-sulfur batteries: electrochemistry, materials, and prospects. *Angew. Chem. Int. Ed. Engl.* 52, 13186–13200.
- Wild, M., O'Neill, L., Zhang, T., Purkayastha, R., Minton, G., Marinescu, M., and Offer, G.J. (2015). Lithium sulfur batteries, a mechanistic review. *Energy Environ. Sci.* 8, 3477–3494.
- Singh, A., and Kalra, V. (2019). Electrospun nanostructures for conversion type cathode (S, Se) based lithium and sodium batteries. *J. Mater. Chem. A* 7, 11613–11650.
- Cheng, X.B., Zhang, R., Zhao, C.Z., and Zhang, Q. (2017). Toward safe lithium metal anode in rechargeable batteries: a review. *Chem. Rev.* 117, 10403–10473.
- Cheng, X.-B., Huang, J.-Q., and Zhang, Q. (2017). Review—Li metal anode in working lithium-sulfur batteries. *J. Electrochem. Soc.* 165, A6058–A6072.
- Li, G., Sun, J., Hou, W., Jiang, S., Huang, Y., and Geng, J. (2016). Three-dimensional porous carbon composites containing high sulfur nanoparticle content for high-performance lithium-sulfur batteries. *Nat. Commun.* 7, 10601.
- He, G., Evers, S., Liang, X., Cuisinier, M., Garsuch, A., and Nazar, L.F. (2013). Tailoring porosity in carbon nanospheres for lithium-sulfur battery cathodes. *ACS Nano* 7, 10920–10930.
- Jayaprakash, N., Shen, J., Moganty, S.S., Corona, A., and Archer, L.A. (2011). Porous hollow carbon@sulfur composites for high-power lithium-sulfur batteries. *Angew. Chem. Int. Ed. Engl.* 50, 5904–5908.
- Ji, L., Rao, M., Aloni, S., Wang, L., Cairns, E.J., and Zhang, Y. (2011). Porous carbon nanofiber-sulfur composite electrodes for lithium/sulfur cells. *Energy Environ. Sci.* 12, 02256C.
- Peng, H.-J., Huang, J.-Q., Cheng, X.-B., and Zhang, Q. (2017). Review on high-loading and high-energy lithium-sulfur batteries. *Adv. Energy Mater.* 7, 1700260.
- Chung, S.H., and Manthiram, A. (2019). Current status and future prospects of metal-sulfur batteries. *Adv. Mater.* 31, e1901125.

15. Pang, Q., Liang, X., Kwok, C.Y., and Nazar, L.F. (2016). Advances in lithium-sulfur batteries based on multifunctional cathodes and electrolytes. *Nat. Energy* **1**, 16132.
16. Tao, X., Wang, J., Ying, Z., Cai, Q., Zheng, G., Gan, Y., Huang, H., Xia, Y., Liang, C., Zhang, W., and Cui, Y. (2014). Strong sulfur binding with conducting Magnéli-phase Ti_2O_{2n-1} nanomaterials for improving lithium-sulfur batteries. *Nano Lett.* **14**, 5288–5294. <https://doi.org/10.1021/nl502331f>.
17. Pai, R., Singh, A., Simotwo, S., and Kalra, V. (2018). In situ grown iron oxides on carbon nanofibers as freestanding anodes in aqueous supercapacitors. *Adv. Eng. Mat.* **20**, 1701116.
18. Pai, R., and Kalra, V. (2018). High performance aqueous asymmetric supercapacitor based on iron oxide anode and cobalt oxide cathode. *J. Mater. Res.* **33**, 1199–1210.
19. Singh, A., and Kalra, V. (2018). TiO Phase Stabilized into Freestanding Nanofibers as Strong Polysulfide Immobilizer in Li-S Batteries: Evidence for Lewis Acid-Base Interactions. *ACS Appl. Mater. Interfaces* **10**, 37937–37947.
20. Peng, H.J., Zhang, G., Chen, X., Zhang, Z.W., Xu, W.T., Huang, J.Q., and Zhang, Q. (2016). Enhanced electrochemical kinetics on conductive polar mediators for lithium-sulfur batteries. *Angew. Chem. Int. Ed. Engl.* **55**, 12990–12995.
21. Pai, R., and Kalra, V. (2021). Vanadium Monoxide-Based Free-Standing Nanofiber Hosts for High-Loading Lithium-Sulfur Batteries. *ACS Appl. Energy Mater.* **4**, 5649–5660. <https://doi.org/10.1021/acsaem.1c00293>.
22. Naguib, M., Kurtoglu, M., Presser, V., Lu, J., Niu, J., Heon, M., Hultman, L., Gogotsi, Y., and Barsoum, M.W. (2011). Two-dimensional nanocrystals produced by exfoliation of Ti₃AlC₂. *Adv. Mater.* **23**, 4248–4253.
23. Sokol, M., Natu, V., Kota, S., and Barsoum, M.W. (2019). On the chemical diversity of the MAX phases. *Trends Chem.* **1**, 210–223.
24. Natu, V., Pai, R., Sokol, M., Carey, M., Kalra, V., and Barsoum, M.W. (2020). 2D Ti₃C₂T_z MXene synthesized by water-free etching of Ti₃AlC₂ in polar organic solvents. *Chem* **6**, 616–630.
25. Anasori, B., Lukatskaya, M.R., and Gogotsi, Y. (2017). 2D metal carbides and nitrides (MXenes) for energy storage. *Nat. Rev. Mater.* **2**, 16098.
26. Verger, L., Natu, V., Carey, M., and Barsoum, M.W. (2019). MXenes: An introduction of their synthesis, select properties, and applications. *Trends Chem.* **1**, 656–669.
27. Zhang, C.J., Anasori, B., Seral-Ascaso, A., Park, S.H., McEvoy, N., Shmeliov, A., Duesberg, G.S., Coleman, J.N., Gogotsi, Y., and Nicolosi, V. (2017). Transparent, flexible, and conductive 2D titanium carbide (MXene) films with high volumetric capacitance. *Adv. Mater.* **29**, 1702678.
28. Ling, Z., Ren, C.E., Zhao, M.Q., Yang, J., Giammarco, J.M., Qiu, J., Barsoum, M.W., and Gogotsi, Y. (2014). Flexible and conductive MXene films and nanocomposites with high capacitance. *Proc. Natl. Acad. Sci. USA* **111**, 16676–16681.
29. Hantanasirisakul, K., Zhao, M.-Q., Urbankowski, P., Halim, J., Anasori, B., Kota, S., Ren, C.E., Barsoum, M.W., and Gogotsi, Y. (2016). Fabrication of Ti₃C₂T_xMXene transparent thin films with tunable optoelectronic properties. *Adv. Electron. Mater.* **2**, 1600050.
30. Carey, M., Hinton, Z., Natu, V., Pai, R., Sokol, M., Alvarez, N.J., Kalra, V., and Barsoum, M.W. (2020). Dispersion and stabilization of alkylated 2D MXene in nonpolar solvents and their pseudocapacitive behavior. *Cell Rep. Phys. Sci.* **1**, 100042.
31. Tang, H., Li, W., Pan, L., Cullen, C.P., Liu, Y., Pakdel, A., Long, D., Yang, J., McEvoy, N., Duesberg, G.S., et al. (2018). In situ formed protective barrier enabled by sulfur/titanium carbide (MXene) ink for achieving high-capacity, long lifetime Li-S batteries. *Adv. Sci. (Weinh.)* **5**, 1800502.
32. Tang, H., Li, W., Pan, L., Tu, K., Du, F., Qiu, T., Yang, J., Cullen, C.P., McEvoy, N., and Zhang, C. (2019). A robust, freestanding mxene-sulfur conductive paper for long-lifetime Li-S batteries. *Adv. Funct. Mater.* **29**, 1901907.
33. Liang, X., Garsuch, A., and Nazar, L.F. (2015). Sulfur cathodes based on conductive MXene nanosheets for high-performance lithium-sulfur batteries. *Angew. Chem. Int. Ed. Engl.* **54**, 3907–3911.
34. Liang, X., Rangom, Y., Kwok, C.Y., Pang, Q., and Nazar, L.F. (2017). Interwoven MXene nanosheet/carbon-nanotube composites as Li-S cathode hosts. *Adv. Mater.* **29**, 1603040.
35. Bao, W., Liu, L., Wang, C., Choi, S., Wang, D., and Wang, G. (2018). Facile synthesis of crumpled nitrogen-doped MXene nanosheets as a new sulfur host for lithium-sulfur batteries. *Adv. Energy Mater.* **8**, 1702485.
36. Song, J., Guo, X., Zhang, J., Chen, Y., Zhang, C., Luo, L., Wang, F., and Wang, G. (2019). Rational design of free-standing 3D porous MXene/rGO hybrid aerogels as polysulfide reservoirs for high-energy lithium-sulfur batteries. *J. Mater. Chem. A Mater.* **7**, 6507–6513.
37. Song, J., Su, D., Xie, X., Guo, X., Bao, W., Shao, G., and Wang, G. (2016). Immobilizing polysulfides with MXene-functionalized separators for stable lithium-sulfur batteries. *ACS Appl. Mater. Interfaces* **8**, 29427–29433.
38. Bao, W., Xie, X., Xu, J., Guo, X., Song, J., Wu, W., Su, D., and Wang, G. (2017). Confined sulfur in 3D MXene/reduced graphene oxide hybrid nanosheets for lithium-sulfur battery. *Chemistry* **23**, 12613–12619.
39. Xiao, Z., Li, Z., Li, P., Meng, X., and Wang, R. (2019). Ultrafine Ti₃C₂ MXene nanodots-interspersed nanosheet for high-energy-density lithium-sulfur batteries. *ACS Nano* **13**, 3608–3617.
40. Ghidui, M., Halim, J., Kota, S., Bish, D., Gogotsi, Y., and Barsoum, M.W. (2016). Ion-exchange and cation solvation reactions in Ti₃C₂MXene. *Chem. Mater.* **28**, 3507–3514.
41. Meyer, B., Austin, J.M., and Jensen, D. (1971). Solubility of sulfur in liquid sulfur dioxide, carbon disulfide, and carbon tetrachloride. *J. Chem. Eng. Data* **16**, 364–366.
42. Fan, F.Y., Carter, W.C., and Chiang, Y.M. (2015). Mechanism and kinetics of Li₂S precipitation in lithium-sulfur batteries. *Adv. Mater.* **27**, 5203–5209.
43. Yang, Y., Zhong, Y., Shi, Q., Wang, Z., Sun, K., and Wang, H. (2018). Electrocatalysis in lithium sulfur batteries under lean electrolyte conditions. *Angew. Chem. Int. Ed. Engl.* **57**, 15549–15552.
44. Guo, D., Ming, F., Su, H., Wu, Y., Wahyudi, W., Li, M., Hedhili, M.N., Sheng, G., Li, L.-J., Alshareef, H.N., et al. (2019). MXene based self-assembled cathode and antifouling separator for high-rate and dendrite-inhibited Li-S battery. *Nano Energy* **61**, 478–485.
45. Dong, Y., Zheng, S., Qin, J., Zhao, X., Shi, H., Wang, X., Chen, J., and Wu, Z.S. (2018). All-MXene-based integrated electrode constructed by Ti₃C₂ nanoribbon framework host and nanosheet interlayer for high-energy-density Li-S batteries. *ACS Nano* **12**, 2381–2388.
46. Zhou, G., Tian, H., Jin, Y., Tao, X., Liu, B., Zhang, R., Seh, Z.W., Zhuo, D., Liu, Y., Sun, J., et al. (2017). Catalytic oxidation of Li₂S on the surface of metal sulfides for Li-S batteries. *Proc. Natl. Acad. Sci. USA* **114**, 840–845.
47. Allen, J., and Bard, L.R.F. (2001). *Electrochemical Methods: Fundamentals and Applications*, Second Edition (Wiley).
48. Zhang, D., Wang, S., Hu, R., Gu, J., Cui, Y., Li, B., Chen, W., Liu, C., Shang, J., and Yang, S. (2020). Catalytic conversion of polysulfides on single atom zinc implanted mxene toward high-rate lithium-sulfur batteries. *Adv. Funct. Mater.* **30**, 2002471.
49. Jiao, L., Zhang, C., Geng, C., Wu, S., Li, H., Lv, W., Tao, Y., Chen, Z., Zhou, G., Li, J., et al. (2019). Capture and catalytic conversion of polysulfides by *in situ* built tio₂-mxene heterostructures for lithium-sulfur batteries. *Adv. Energy Mater.* **9**, 1900219.
50. Liu, D., Zhang, C., Zhou, G., Lv, W., Ling, G., Zhi, L., and Yang, Q.H. (2017). Catalytic effects in lithium-sulfur batteries: promoted sulfur transformation and reduced shuttle effect. *Adv. Sci. (Weinh.)* **5**, 1700270.
51. Cañas, N.A., Wolf, S., Wagner, N., and Friedrich, K.A. (2013). *In-situ* X-ray diffraction studies of lithium-sulfur batteries. *J. Power Sources* **226**, 313–319.